STUDY OF CFD METHODS APPLIED TO RAPIDLY DEFORMING BOUNDARIES

John W. Slater*
NASA Lewis Research Center, Cleveland, Ohio
and
Donald Freund† and Miklos Sajben‡
Department of Aerospace Engineering and Engineering Mechanics
University of Cincinnati, Cincinnati, Ohio

Abstract

A study of various methods of computational fluid dynamics (CFD) was performed to understand their effects on the analysis of the flow field induced by the rapid collapse of a flexible bump in an annular duct with initially stagnant conditions. This flow represents a good test case for CFD methods for deforming boundaries because the flow is due entirely to the boundary motion. The study examined methods for implementing explicit and implicit time integration, modeling the bump collapse, imposing moving surface boundary conditions, modeling the grid dynamics, computing the numerical flux, and imposing the geometric conservation law. Good agreement was obtained between the CFD results and the time-varying static pressure readings obtained from an experiment. Significant results showed the crucial importance of the bump collapse model and the wall boundary conditions. The geometric conservation law was not of critical importance.

Introduction

The methods of computational fluid dynamics (CFD) are increasingly being applied to problems involving the relative motion of the boundaries of a flow domain[1]. The significance of the boundary motion on the flow is determined by the amount of momentum transfer between the moving boundary and the fluid. This is determined by the velocity of the moving boundary with respect to the velocity of the local flow and the spatial extent of the moving boundary. As an example, consider an object being dropped from an aircraft traveling at Mach 0.6. In a stable release, the vertical speed of the object relative to the aircraft is determined by gravitational acceleration. At one meter from the aircraft, the vertical speed of the object is about 3% of the freestream velocity of the fluid. Another example is a high-speed, variable geometry inlet which involves centerbody motion occurring over a one second time interval. If the throat Mach number is 1.2, the speed of the centerbody surfaces relative to the fluid speed is less than 1% of the fluid speed.

The focus of this paper is on rapid boundary motion in which the speed of the boundary motion approaches the speed of the fluid motion. CFD methods for moving boundaries are considerably challenged since the moving boundary has a significant influence on the flow.

Recently, experiments were conducted at the University of Cincinnati as part of an effort to design a mechanism capable of creating a planar pressure pulse within an annular duct through the rapid collapse of a flexible bump located on the hub of the duct[2,3]. The overall objective was the investigation of the interaction of the pulses with the compressor fan of a jet engine in which the mean flow at the compressor face is approximately Mach 0.2. During the design of the pulse generation concept, CFD methods were approached to validate the concept; however, it was unsure if the CFD methods themselves were verified to produce accurate results. Thus, a lower cost experiment was designed in which the bump collapse occurred in stagnant conditions (no mean flow) in an annular duct. Thus any flow that was induced was totally due to the bump collapse. The time histories of the pressure at a few locations

*Aerospace Engineer, Inlet Branch, AIAA Senior Member
†Graduate Assistant, AIAA Student Member
‡Professor, Ohio Eminent Scholar, AIAA Fellow

along the duct were collected and compared to the CFD results. The comparisons were very good and the results have been presented in an earlier paper[3]. Thus, the CFD methods were verified for the problem and could then be used with confidence to validate the design concept of the actual pulse generator at the design conditions with mean flow.

One objective of this paper is to promote the experiment data as a test case for CFD codes with deforming boundary capability. Another objective is the understanding of the sensitivities of specific CFD methods used for the analysis. The CFD methods were coded into the programs DGNS2D[4] and NPARC2D-DG[5] to solve the unsteady, compressible Navier-Stokes equations. These codes and their respective CFD methods of particular importance to the deforming boundary capability are discussed. Several sensitivity studies are discussed which investigated methods for implementing explicit and implicit time integration, modeling the bump collapse, imposing moving surface boundary conditions, modeling the grid dynamics, computing the numerical flux, and imposing the geometric conservation law. The fairly simply geometry of the cases considered in this paper allows the use of a single-block, structured grid which deforms. The cases involve a rapidly moving piston, for which an analytic solution is known, and a collapsing bump in a duct, which is compared to the experiment data.

Flow Equations

The integral form of the Navier-Stokes equations for a time-varying, axisymmetric control volume of one radian are

$$\hat{Q}_t + \hat{R} = \hat{S} \tag{1}$$

where t is time and

$$\hat{Q} = \int_{V(t)} Q \, dV \quad \text{and} \quad \hat{R} = \oint_{S(t)} \mathbf{H} \cdot \hat{n} \, dS.$$

The V is the volume and S is the surface of the control volume. The $\hat{n}$ is the surface normal vector. The surface integrals for $\hat{R}$ are only for the axial and radial surfaces of the axisymmetric control volume. The $\hat{S}$ is the axisymmetric source term

$$\hat{S}^T = S_\theta \, (\, 0, \, 0, \, p, \, 0 \,) \tag{2}$$

which accounts for the surface integrals for the circumferential surfaces of the control volume. The S_θ is the area of the circumferential plane. The p is the static pressure. The Q is the algebraic vector of conservative variables

$$Q^T = \left(\rho, \, \rho \vec{V}, \, E_t \right) \tag{3}$$

where ρ is the density, $\vec{V} = u \, \hat{\imath} + v \, \hat{\jmath}$, and u and v are the axial and radial flow velocity components, respectively. The E_t is the total energy per unit volume

$$E_t = \frac{p}{\gamma - 1} + \frac{1}{2} \rho \, \vec{V} \cdot \vec{V} \tag{4}$$

The $\mathbf{H}$ is the flux dyadic, which for a mixed Eulerian-Lagrangian description[6] is,

$$\mathbf{H} = \mathbf{F} - \vec{g} \, Q. \tag{5}$$

The $\vec{g}$ is the velocity vector for the axial and radial control surfaces, $\vec{g} = x_t \hat{\imath} + y_t \hat{\jmath}$, which is also known as the grid speed vector. An Eulerian description is obtained for $\vec{g} = 0$ while a Lagrangian description is obtained for $\vec{g} = \vec{V}$. The $\mathbf{F}$ is the Cartesian flux dyadic. The x_t and y_t are the axial and radial grid speeds, respectively. The flow model is complete with Sutherland's formula, the definition of the Prandtl number, and a perfect gas assumption. For the present work, turbulence is not significant. The specification of boundary conditions and an initial solution then close the system of equations.

Computational Methods

The CFD methods were coded into the DGNS2D and NPARC2D-DG codes.

DGNS2D

The DGNS2D[4] code solves for the cell-vertex, finite-volume representation of Eq.(1) in which

$$\hat{Q} = V \, Q \quad \text{and} \quad \hat{R} = \sum_f \hat{F}_f$$

where the index f is over the axial and radial faces of the axisymmetric control volume and where

$$\hat{F} = \mathbf{H} \cdot \hat{n} \, dS \tag{6}$$

which is evaluated at the cell face f.

A second-order time-integration is performed through the two-stage Lax-Wendroff method[7]

$$\hat{Q}^* = \hat{Q}^n - \Delta t \left(\hat{R}^n - \hat{S}^n \right), \tag{7}$$

$$\hat{Q}^{**} = \hat{Q}^* - \Delta t \left(\hat{R}^* - \hat{S}^* \right), \tag{8}$$

and

$$\hat{Q}^{n+1} = \frac{1}{2} \left(\hat{Q}^n + \hat{Q}^{**} \right) \tag{9}$$

where n, $*$, and $**$ are the time-level indices.

Roe's upwind flux-difference splitting method, as implemented in Ref. 7, is used to evaluate $\hat{F}$ with

modifications for a moving cell face. Thus $\hat{F}$ is evaluated at the cell face as

$$\hat{F} = \sum_{m=1}^{4} \lambda_m \, \hat{\vec{r}}_m \, \hat{\vec{l}}_m^{\,T} \, \hat{Q} \qquad (10)$$

where $\hat{\vec{r}}_m$ and $\hat{\vec{l}}_m$ are the right and left eigenvectors, respectively. The λ_m are the eigenvalues and are the only portion of the flux which contains the grid speeds. The eigenvalues have the form

$$\lambda_1 = \lambda_2 = \left(\vec{V} - \vec{g} \right) \cdot \hat{n} \qquad (11)$$

and

$$\lambda_{3,4} = \left(\vec{V} - \vec{g} \right) \cdot \hat{n} \pm c \qquad (12)$$

where c is the local speed of sound.

The explicit method uses the CFL condition to determine the maximum stable time step

$$\Delta t = \frac{\nu \, \Delta s}{| \lambda_m |_{max}} \qquad (13)$$

where ν is the CFL number and Δs represents the grid spacing of the cell. The grid speeds influence the time step through the presence of the eigenvalues.

NPARC2D-DG

The NPARC2D-DG[5] code was developed from version 2.0 of the NPARC2D[8,9] code to efficiently solve unsteady, viscous, turbulent flows. NPARC2D uses a finite-difference representation of Eq.(1) in strong conservation form in which

$$\hat{Q} = Q / J \quad \text{and} \quad \hat{R} = \frac{\partial \hat{F}_j}{\partial \xi_j}.$$

The generalized flux components for a time-varying grid are

$$\hat{F}_j = \frac{1}{J} \left(\frac{\partial \xi_j}{\partial t} Q + \frac{\partial \xi_j}{\partial x_k} F_k \right) \qquad (14)$$

where the generalized and physical coordinates are $\xi_j \in (\xi, \eta)$ and $x_j \in (x, y)$, respectively. A transformation exists between (τ, ξ, η) and (t, x, y) in which $\tau = t$. The metrics of the axisymmetric transformation are

$$\xi_t = - x_\tau \xi_x - y_\tau \xi_y, \quad \eta_t = - x_\tau \eta_x - y_\tau \eta_y,$$

$$\xi_x = y \, y_\eta \, J, \quad \eta_x = - y \, y_\xi \, J,$$

$$\xi_y = - y \, x_\eta \, J, \quad \eta_y = y \, x_\xi \, J,$$

where J is the axisymmetric Jacobian of the transformation

$$J^{-1} = (x_\xi \, y_\eta - x_\eta \, y_\xi) \, y. \qquad (15)$$

The finite-difference equations are approximated spatially through the use of a second-order, central-difference. The viscous fluxes are evaluated explicitly. No second-order artificial dissipation was used for the flows discussed in this paper. NPARC uses a pentadiagonalized approximate-factorization of the Euler implicit time difference. NPARC2D-DG uses a three-point, backwards time difference with a Newton sub-iteration procedure to provide for nominally second-order time accuracy. Such a procedure has been presented in several references[10,11,12]. The iterative equation assuming a constant time step is

$$\left[I + \frac{2\Delta\tau}{3} \frac{\partial \hat{A}^m}{\partial \xi_j} \right] \Delta \hat{Q}^m = - \frac{2\Delta\tau}{3} \left(\hat{R}^m - \hat{S}^m \right) - \left(\hat{Q}^m - \frac{4}{3} \hat{Q}^n + \frac{1}{3} \hat{Q}^{n-1} \right) \qquad (16)$$

where $\hat{A}$ is the Jacobian of $\hat{F}$. The m is the sub-iteration index.

The Newton iterative procedure takes advantage of the existing NPARC solver with minor modifications. Eq.(16) is iterated at each time step until the right-hand-side essentially becomes zero, which assures that the finite-difference form of Eq.(1) is satisfied. This generally requires only a few sub-iterations at each time step since the initial solution is usually close to the solution at the new time. Essentially, second-order time-accuracy is obtained through the sub-iterations even though the diagonalization is not time-accurate. Further time-accuracy issues are discussed in detail by Pulliam[10].

Flow Boundary Conditions

For both codes, the boundary conditions are imposed explicitly. The multi-stage and sub-iteration procedures reduce the errors in the temporal accuracy at the boundaries.

The flow boundary condition at the solid wall is the mechanism through which the flow senses that a boundary is in motion. The inclusion of the grid speed vector $\vec{g}$ accounts for the motion of the boundary. The single physical flow boundary condition for a slip solid wall is

$$\rho \left(\vec{V} - \vec{g} \right) \cdot \hat{n} = 0 \qquad (17)$$

which is a statement that the component of the fluid velocity in the direction of the surface normal vector $\hat{n}$ must match the component of the grid speed vector in the direction of the surface normal vector. An

additional physical boundary condition that exists with the case of a no slip wall is

$$\rho \left(\vec{V} - \vec{g} \right) \cdot \hat{t} = 0 \qquad (18)$$

which with Eq.(17) results in the condition

$$\vec{V} = \vec{g}. \qquad (19)$$

For the case of the flow about the collapsing bump, the inflow and outflow boundaries for the duct were specified as fixed conditions since the short physical times considered in this work do not result in an interaction of the flow in the region of sensor C (see below) with waves reflected from the duct ends.

Geometric Conservation Law

The deformation of the grid is a source of possible errors. One must require that a uniform flow be preserved independent of the grid motion. This is stated in the geometric conservation law[13] which essentially relates the change in volume of the cell to the motion of the cell faces,

$$\frac{dV}{dt} = \oint_{S(t)} \vec{g} \cdot \hat{n} dS. \qquad (20)$$

For the finite-volume representation used in DGNS2D, Eq.(20) is solved using the two-stage, Lax-Wendroff method to obtain V_{GCL}^{n+1}. The solution at time level $(n+1)$ is then decoded as

$$Q^{n+1} = \hat{Q}^{n+1} \; / \; V_{GCL}^{n+1}. \qquad (21)$$

The geometric conservation law for the finite-difference form of Eq.(1) is

$$(J^{-1})_\tau = - \left[(\xi_\tau / J)_\xi + (\eta_\tau / J)_\eta \right]. \qquad (22)$$

Applied to the Newton sub-iteration method, the GCL can be used to find the Jacobian which yields uniform flow

$$(J^{-1})_{GCL}^{n+1} = \frac{4}{3} (J^{-1})^n - \frac{1}{3} (J^{-1})^{n-1} + \frac{2\Delta\tau}{3} (J^{-1})_\tau^{n+1}. \qquad (23)$$

At each sub-iteration, the new value of $\hat{Q}$ can be evaluated as

$$\hat{Q}^{n+1} = \hat{Q}^{n+1} \; J_{GCL}^{n+1} \; / \; J_{GRID}^{n+1} \qquad (24)$$

where J_{GRID}^{n+1} is the Jacobian as computed from the known grid at time level $(n+1)$. The new solution is then decoded as

$$Q^{n+1} = \hat{Q}^{n+1} \; J_{GRID}^{n+1}. \qquad (25)$$

Grid Regeneration and Dynamics

The collapse of the bump in the duct requires a deformation of the single-block, structured grid at each time step. An automated grid generation procedure is used in which the grids are generated at all times during the analysis based on inputs of the geometry model, grid topology, grid quality parameters, and flow boundary conditions[4]. The single grid block is divided into three axial sub-blocks with one of the sub-blocks located at the bump. The grid regeneration is localized to the sub-block containing the bump. The generation of the interior grid is performed efficiently through the use of an algebraic, transfinite interpolation method applied for each sub-block. The grid speeds are computed from a first-order, backwards time difference of the grids. At the start of the computation, a transfinite interpolation of the boundary grid speeds is used since no previous grid exists for the time difference.

Moving Piston Expansion

A simple test case involving a deforming boundary is a straight duct 10 meters long with its right boundary moving to the right at a constant speed of 100 m/sec, which may simulate the motion of a piston. A centered expansion wave is formed at the piston surface and propagates into the duct. The method of characteristics provides for an analytic solution for the flow properties with respect to space and time[14]. In the CFD computation, the entire grid deforms axially as the wall is moved. The computation was performed with both codes to a final time of $t_f = 0.01$ sec. Fig. 1 presents a comparison of the spatial variation in density in the duct at the final time. Both codes performed well with regards to the time accuracy; however NPARC2D-DG was slightly more dissipative and introduced oscillations at the tail of the expansion. Both computations used a constant time step of $\Delta t = 1.25$E-05 seconds and a grid with 502 axial and 51 radial grid points.

Rapid Collapse of a Bump

The objective of this case was the generation of an individual, well-characterized, short-duration acoustic pulse of amplitude of 5-10% of the ambient pressure. The case involves an axisymmetric bump formed on the hub of a constant-area annulus. The bump collapses within one milli-second (msec) to form a cylindrical section flush with the hub. Two expansion pulses are formed - each traveling axially at the speed of sound away from the bump. As they travel along the duct, they form a planar structure.

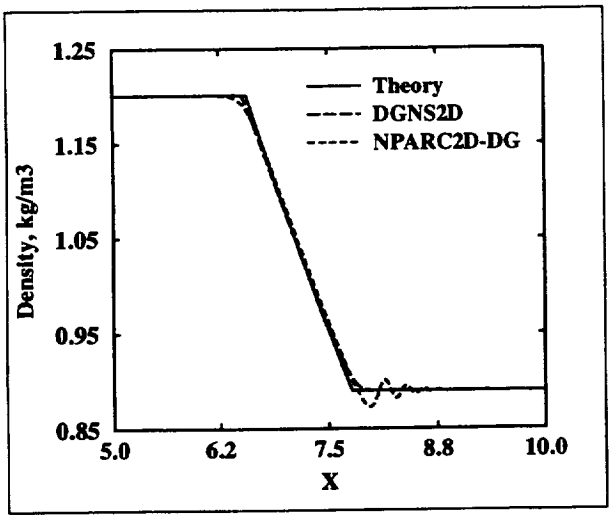

Figure 1: **The spatial variation of density through a centered expansion wave generated by a rapidly moving piston.**

Description of the Experiment

A diagram of the experiment test rig designed and built at the University of Cincinnati is shown in Fig. 2. The hub is a smooth steel pipe and the case is a smooth acrylic (Lexan) pipe. The length of the annulus is 127 cm. The static pressures in the duct were measured at three locations, labeled A, B, and C in Fig. 2, using high-response pressure transducers with a sampling speed of 100 kHz per channel. The sensor location C is 24 channel heights from the center of the bump and represents the distance at which a well-characterized pulse is desired (i.e. distance to a compressor face).

The bump has a length of 9.5 cm and is formed by the deformation of a thin-walled silicon rubber (RTV) tube segment (called the "boot"). The deformation is due to the pressurization of the driver section of a shock tube within the hub. A wire cage which is flush to the hub supports the "boot" to form a cylindrical section when the driver pressure is at or below ambient conditions. The height at the center of the bump can be adjusted by the level of pressurization. The collapse of the bump occurs when the diaphragm of the shock tube is burst by the actuation of a spear mechanism. When helium is used as the driver gas, bump collapse times of less than 1.0 msec are observed.

Two bump heights are considered in this work: the first one has a ratio of bump height h to duct height H of $h/H = 0.26$ and the second has a ratio of $h/H = 0.50$. Fig. 3 shows the initial shape of these bumps as mechanically measured at a series of axial stations.

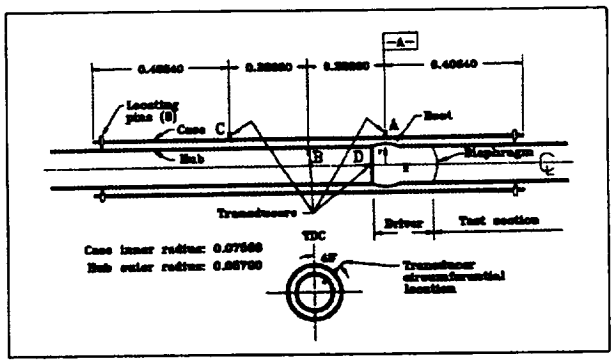

Figure 2: **The experiment setup and transducer locations for the duct with a rapidly collapsing bump.**

The variation in time of the height of the center of the bump was measured using an optical laser system and the following relation was produced for times up to the collapse time

$$h(t) = h_{t=0}\left[\cos\left(\frac{\pi\, t}{2\, T}\right)\right]^{0.8} \qquad (26)$$

where T is the collapse time. Fig. 4 shows the behavior of this relation. The 26% and 50% bumps have collapse times of $T = 0.6$ msec and $T = 0.8$ msec, respectively.

The variation of the shape along the rest of the bump during the collapse was not measured; however, it was felt by intuition that the bump collapses with a uniform displacement at each differential time increment (uniform velocity). This would result in the ends of the bump reaching the hub first with the collapse moving in toward the center of the bump.

For the bump collapse occurs in initially stagnant conditions (no flow). Thus, the induced flow and generated pulses are due entirely to the bump motion without being superimposed on a mean flow. Figs. 5 and 6 show the recorded static pressures at sensor location C for the 26% and 50% bumps, respectively. The filled circles represent every other data point observed by the transducers. Pulses were generated with amplitudes of approximately 6% and 10% of the ambient static pressure, respectively. After the main pulse has passed, a smaller, decaying oscillation is noticed, which is believed due to the drum-like vibration of the boot and the possible rebounding of the boot from the hub.

Reference CFD Solution

The experiment described above represents a good test case for CFD codes with a deforming grid capability because the geometry is fairly simple and since flow conditions are initially stagnant, the ini-

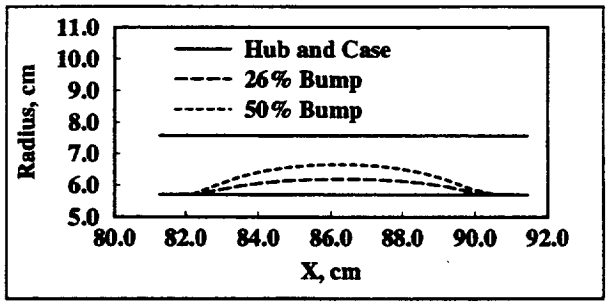

Figure 3: **The initial shape of the 26% and 50% height bumps in the duct.**

tial conditions for the computation are known exactly. The short times involved reduce the influence of the flow boundary conditions at the ends of the duct and emphasize the influence of the moving solid wall boundary conditions.

An earlier paper[3] discussed the accuracy of the experiment data and comparisons with CFD results using DGNS2D. It was determined that the experiment data were highly reproducible and axisymmetric. The CFD results compared well with the experiment data with respect to the amplitude and motion of the pulse at the three sensor locations for both the 26% and and 50% bump heights.

The computations presented here only compare the CFD results and experiment data at sensor location C. Since sensor C is the furthest sensor from the bump, it involves a longer propagation time, and so, a longer computation time. Thus it demands the most from the CFD computation.

The cases were simulated using DGNS2D and NPARC2D-DG using a variety of grid densities, time steps, and CFD methods. Those studies are presented in the following sections. Here, we present a set of solutions to be used as the reference for those studies. A uniformly spaced grid of 837x14 was used for the 26% bump height case and a grid of 838x14 was used for the 50% bump height case. A uniform, constant time step of $\Delta t = 0.001$ msec was used for both cases to march in time from a time of $t = 0.0$ msec to a time of $t = 3.0$ msec. Figs. 5 and 6 show the comparison between the experiment and computed time histories of pressures at sensor location C. The comparisons are very good; however, the head of the expansion is computed to be sharper than in the experiment. The reason for this is not known. The bump collapse model used in the computations does not simulate the rebound of the boot from the hub, and so, the larger oscillations after the main pulse are not present in the computed results.

The above computations assume that viscosity is not significant. A computation of the 50% bump

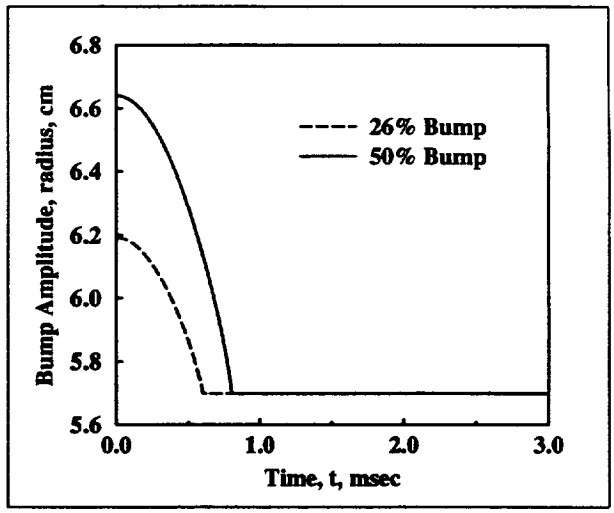

Figure 4: **The variation of the bump amplitude (height of the center of the bump) with time.**

height case was performed using DGNS2D in which laminar viscosity is included. Fig. 7 shows the comparison of the time history of the computed static pressures with experiment data. The effect of the viscosity is to diminish slightly the amplitude of the pulse, which is consistent with the dissipative nature of fluid viscosity.

Since viscosity has only a minor effect, the remaining computations assume inviscid flow conditions. Further, only the 50% bump height case will be examined since it is the higher energy flow.

Characteristic Quantities of the Flow

The studies discussed below require characteristic quantities of the flow in addition to the plot of the time history of the static pressures. One characteristic quantity was obtained from the time integration of the static pressure at sensor C,

$$I = \int_{t=0.0}^{t=3.0} p(t)\, dt. \qquad (27)$$

This quantity can be regarded as an impulse (per unit area) of the pulse between the initial and final times and is a measure of the energy of the pulse. Another characteristic quantity is the time at which the pulse returns to a pressure of 0.985 atm and is noted as the arrival time, t^*. This quantity measures the phase or position of the pulse. The reference values (I_{ref}, t^*_{ref}) are computed from the CFD solutions for each code presented in Fig. 6. These two characteristic quantities represent the strength and speed of the pulse.

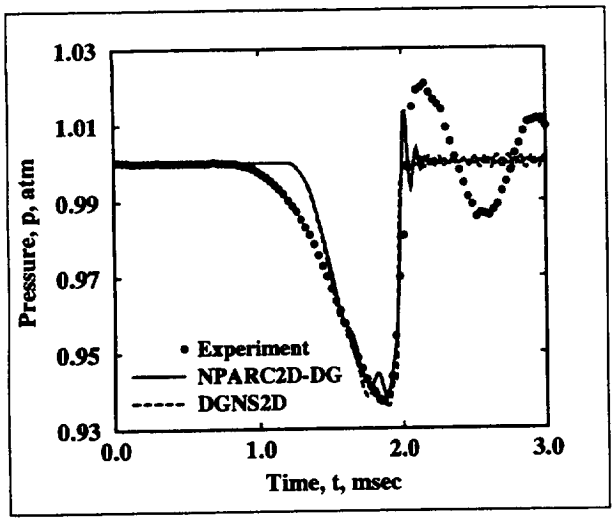

Figure 5: **The time history of the static pressure at sensor C for the 26% bump case.**

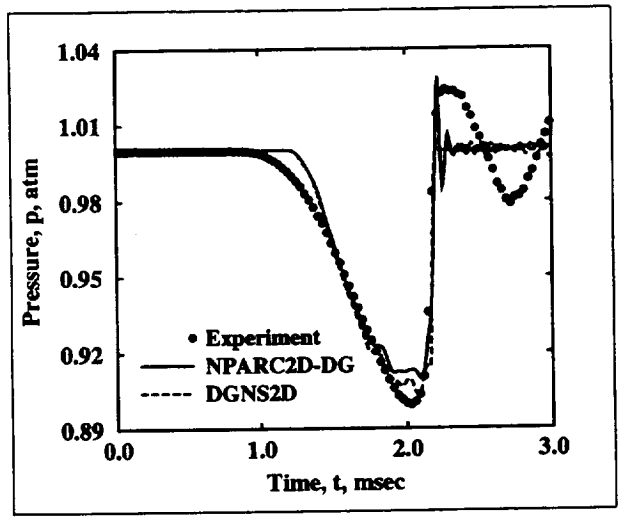

Figure 6: **The time history of the static pressure at sensor C for the 50% bump case.**

Grid Resolution Study

A grid resolution study was performed using DGNS2D in the manner suggested by Roache[15]. The grid convergence index G is a measure of the variability of a characteristic quantity of the solution as the grid spacing is changed and is presented as a percentage computed as

$$G = \frac{3\,|\epsilon|\,r^p}{(r^p - 1)}\,100\% \qquad (28)$$

where the relative error ϵ is computed as

$$\epsilon = (\,f_c - f_f\,)\,/\,f_f. \qquad (29)$$

The f is the characteristic quantity, which here is either the impulse I or the arrival time t^*. The p is the order of the numerical methods, which for this work is taken as $p = 2$. The r is the grid refinement ratio which for this work is defined as $r = \Delta x_c\,/\,\Delta x_f$, where Δx is the axial grid spacing and the subscripts c and f denote the coarser and finer grids, respectively. A series of six uniformly-space grids were used to perform the analyses. The same spacing was used in the radial direction as the axial direction, and so, $\Delta x = \Delta y$. A uniform, constant time step of $\Delta t = 0.001$ msec was used. Table 1 shows the results of the grid resolution study.

Table 1. The results of the grid resolution study for the 50% bump case (DGNS2D).

$\Delta x/H$	I	$G_I(\%)$	t^*	$G_{t^*}(\%)$
0.0676	0.8534	2.276	2.1779	0.661
0.0812	0.8505	0.727	2.1800	0.015
0.0947	0.8512	9.614	2.1799	0.036
0.1083	0.8596	0.799	2.1799	1.053
0.1218	0.8602	25.371	2.1819	1.246
0.1352	0.8770		2.1840	

The grid convergence indices were quite low for grid spacings of $\Delta x\,/\,H = 0.0947$ and 0.0812, which provided confidence that the flow fields were in the asymptotic range of convergence and that the computed measures were within a couple of percent of the asymptotic numerical value. Based on this, the computations below using both DGNS2D and NPARC2D-DG use these grid spacing factors.

Only slight differences were noticed at the maximum magnitude of the pulse for the grids. The increased grid resolution predicts less of an amplitude for the pulse and brings out some small scale oscillations after the main pulse has passed.

Time Resolution Study

A time resolution study was performed in an analogous manner as that for the grid resolution. A grid spacing of $\Delta x\,/\,H = 0.0947$ was used for the analyses with constant, uniform time steps of $\Delta t = 0.0012$ msec, 0.001 msec, and 0.0008 msec. Table 2 shows the results. There is essentially no difference in the results and it is expected that the time steps provide for good time resolution for both DGNS2D and NPARC2D-DG.

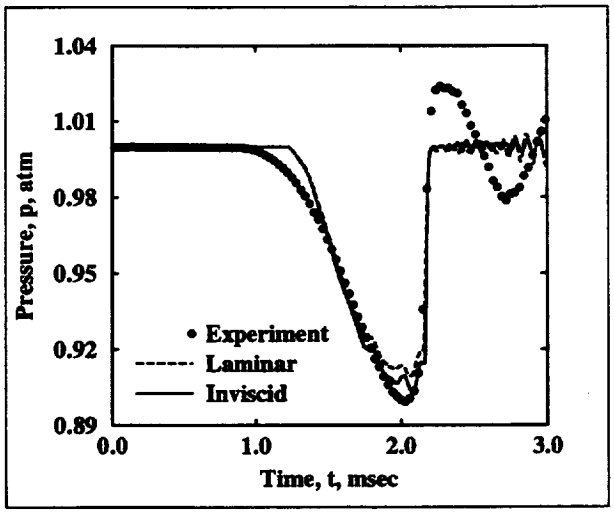

Figure 7: **The influence of viscosity on the time history of the static pressure at sensor C for the 50% bump case using DGNS2D.**

Table 2. The results of the time resolution study for the 50% bump case (DGNS2D).

$\Delta\tau$ (msec)	I	$G_I(\%)$	t^*	$G_{t^*}(\%)$
0.0008	0.8513	0.057	2.1791	0.203
0.0010	0.8512	0.059	2.1799	0.286
0.0012	0.8517		2.1790	

Sensitivities

Sensitivity studies were performed to evaluate the influence of specific CFD methods in obtaining an accurate simulation of the bump collapse. The sensitivities (S_I, S_t) are defined as a percentage of error from the reference values (I_{ref}, t^*_{ref}),

$$S_I = \left(\frac{I - I_{ref}}{I_{ref}}\right) 100\% \qquad (30)$$

and

$$S_t = \left(\frac{t^* - t^*_{ref}}{t^*_{ref}}\right) 100\%. \qquad (31)$$

The following sections discuss the sensitivity studies.

Bump Collapse Model Study

It was mentioned above that the shape of the bump as it collapsed was not directly measured, but that it was estimated to collapse with a uniform displacement, which is equivalent to a uniform vertical velocity over the length of the bump. However, the velocity does vary according to the time variation of the bump height presented in Eq.(26). This model is termed the uniform displacement model and was coded into the CFD codes with good results, as shown in Figs. 5 and 6.

A study was performed using DGNS2D to determine the sensitivities of the computed solutions on the choice of the bump collapse model. Two alternative models were studied. The first alternative model was a "proportional displacement" model which assumed that the bump collapsed in proportion to the local initial bump height. Thus, the entire length of the bump would reach the hub surface at the specified collapse time. The second alternative model was a "linear displacement' model which assumed that the displacement was uniform over the length of the bump, but was at a constant velocity with respect to time.

The sensitivities obtained using the "proportional displacement" model are presented in Table 3 as study A. The sensitivities obtained using the "linear displacement" model are presented in Table 3 as study B. The sensitivities are low; however, if one looks at Fig. 8, the differences are more clearly seen. Although these two alternative models are not good choices, it is clear that the solution is sensitive to the choice of the bump collapse model.

Table 3. The sensitivities of the impulse and arrival time with respect to specific CFD methods. (N/A - not applicable)

	DGNS2D		NPARC2D-DG	
Study	S_I	S_t	S_I	S_t
A)	-0.346	1.836	-	-
B)	-0.096	-3.669	-	-
C)	-100.0	-100.0	-100.0	-100.0
D)	62.163	1.643	67.776	4.145
E)	-7.316	0.047	-	-
F)	0.080	-0.021	-0.024	0.003
G)	N/A	N/A	1.345	1.851
H)	3.908	0.099	-3.761	-0.099

A) Proportional displacement collapse model
B) Linear displacement collapse model
C) No use of the grid speeds in the BCs
D) Neglect of the grid speeds in the flux
E) Use of a first-order flux formula
F) No use of the geometric conservation law
G) Use of only 1 sub-iteration rather than 3
H) Difference in DGNS2D and NPARC2D-DG

Flow Boundary Condition Study

A study was performed using both DGNS2D and NPARC2D-DG to determine the sensitivities of the computed solutions to the use of the grid speeds in the solid wall boundary conditions. Study C determined that if the grid speeds are totally neglected in

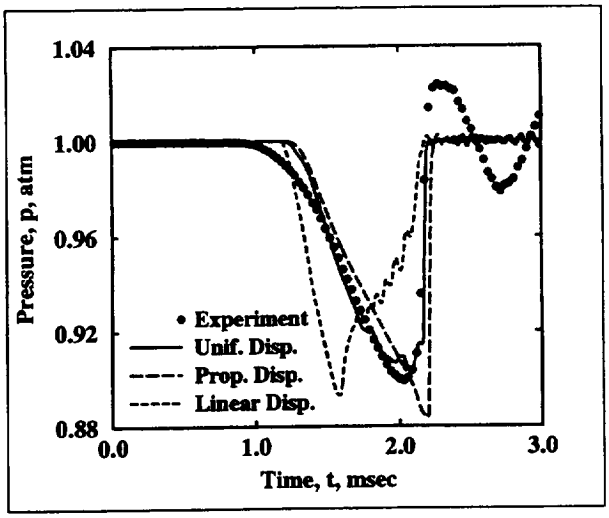

Figure 8: **The influence of the bump collapse model on the time history of the static pressure at sensor C for the 50% bump case.**

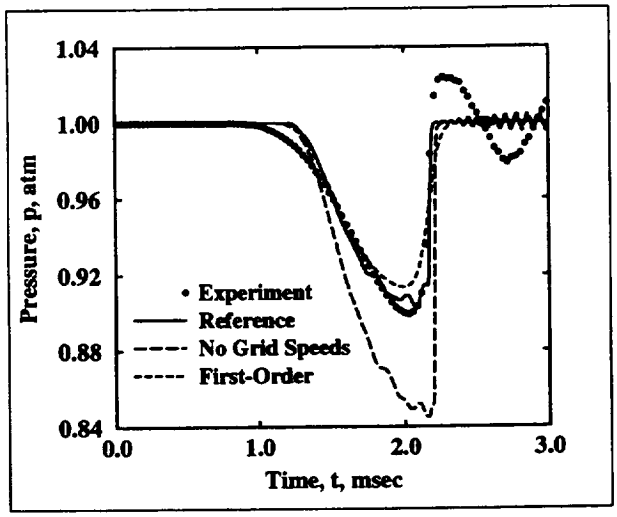

Figure 9: **The influence of the flux methods on the time history of the static pressure at sensor C for the 50% bump case using DGNS2D.**

the boundary conditions, the flow remains stagnant. The sensitivities of Table 3 are then -100%. When using DGNS2D, it was also found that using a first-order extrapolation of variables at the boundary, as opposed to using a zero-order extrapolation, had no effect on the computed results. This was also true when the curvature of the boundary was modeled when determining the value of the wall pressure.

Flux Method Study

Study D determined the sensitivities to neglecting the grid speeds in the flux computations of DGNS2D and NPARC2D-DG. As seen in Table 3 for both codes and the plot of Fig. 9 for DGNS2D, there is significant error with amplitude of the pulse being overpredicted.

Study E determined the sensitivities of using just the first-order flux formula of Roe's flux-difference splitting in DGNS2D. The result, as shown in Fig. 9, was a predictable dissipation of the amplitude of the pulse; however, the time-accuracy remained good. Further, the higher-order oscillations are damped.

Geometric Conservation Law Study

Study F determined the sensitivities to the use of the geometric conservation law. The sensitivities of Table 3 show that the exclusion of the geometric conservation law had negligible effect for either code. This result did not change when larger time steps were used for the computation, which would result in a greater change in cell volume per time step. The largest time steps examined resulted in a degraded solution, and so, did not represent suitable time steps for the computation. The insensitivity of the geometric conservation law can partially be explained in that the maximum cell deformation involves a change in volume of 39uniform cell volume at the end of the bump collapse when the grid is uniform. Thus for the largest time steps, the maximum volume change per time step was at most 0.41

Sub-iteration Study

Study G determined the sensitivities to the number of sub-iterations used in the implicit method of NPARC2D-DG. Table 3 shows that there was only a slight difference in the sensitivities between the use of 1 sub-iteration per time step to the use of 3 sub-iterations per time step. This could be due to the fact that the time step used was already small enough to assure good time accuracy.

DGNS2D / NPARC2D-DG Study

Study H determined the sensitivities to the choice of DGNS2D or NPARC2D-DG. The sensitivities to the use of DGNS2D were computed using the results of the NPARC2D-DG solution as the reference, and vice-versa for the sensitivities for NPARC2D-DG. Table 3 shows that the differences between the DGNS2D and NPARC2D-DG were fairly small.

Grid Regeneration Efficiency

The sub-blocking of the grid results in only about 7.2% of the grid (the grid near the bump) being regenerated at each time step. A linear relationship has been observed between the grid dynamics level (percentage of regenerated grid points) and the amount of additional CPU time required for the grid regeneration. A 100% grid regeneration level

required about 89% more CPU time. Thus, a 7.2% grid regeneration level only required 6.4% more CPU time.

Summary and Conclusions

The experiment described provides a good test case for CFD codes with a deforming boundary capability because the fluid motion is due entirely to the deforming boundary. Further, the geometry and initial and boundary conditions are fairly simple. Sensitivity studies were performed to understand the importance of specific CFD methods for the accurate simulation of the flow. Of primary importance were the bump collapse model, solid wall boundary conditions, and flux computation. The geometric conservation law was not of critical importance for the conditions of this problem.

References

[1] Sakell, L. and Knight, D.D., Editors, *Proceedings of the First AFOSR Conference on Dynamic Motion CFD*, June 1996.

[2] Sajben, M. and D.D. Freund, "Experimental Exploration of Compressor-Face Boundary Conditions for Unsteady Inlet Flow Computations," AIAA Paper 95-2886, July 1995.

[3] Freund, D.D., Sajben, M., and Slater, J.W., "Compressor-Face Boundary Condition Experiment: Generation of Acoustic Pulses in Annular Ducts," AIAA Paper 96-2657, July 1996.

[4] Slater, J.W., "A Combined Geometric Approach for the Navier-Stokes Equations on Dynamic Grids," Proceedings of the ICFD Conference, Oxford University Press, April 1995.

[5] Slater, J.W., "Efficient Computation of Unsteady Planar Internal Viscous Flows with Moving Geometry," AIAA Paper 96-0113, January 1996.

[6] Vinokur, M., "An Analysis of Finite-Difference and Finite-Volume Formulations of Conservation Laws," *Journal of Computational Physics*, Vol. 81, 1989, pp. 1-52.

[7] Liou, M.-S. and A.T. Hsu. "A Time-Accurate Finite Volume High Resolution Scheme for Three Dimensional Navier-Stokes Equations," AIAA Paper 89-1994, June 1989.

[8] Cooper, G.K. and Sirbaugh, J.R., "The PARC Code: Theory and Usage," AEDC-TR-89-15, December 1989.

[9] "NPARC Version 2.0 User's Manual", November 1994.

[10] Pulliam, T.H., "Time Accuracy and the Use of Implicit Methods," AIAA Paper 93-3360, July 1993.

[11] Chung, Joongkee and G.L. Cole, "Comparison of Compressor Face Boundary Conditions for Unsteady CFD Simulations of Supersonic Inlet," AIAA Paper 95-2627, July 1995.

[12] Rigby, D.L., "Compact Spatial Differencing and Subiteration Time Marching in the PARC Code," AIAA Paper 96-0385, January 1996.

[13] Thomas, P.D. and Lombard, C.K., "Geometric Conservation Law and its Application to Flow Computations on Moving Grids," *AIAA Journal*, Vol. 17, No. 10, 1979, pp. 1030-1037.

[14] Anderson, J.D., *Modern Compressible Flow*, McGraw Hill Inc., New York, 1984.

[15] Roache, P.J., "Perspective: A Method for Uniform Reporting of Grid Refinement Studies," *Journal of Fluids Engineering*, Vol. 116, September 1994, pp. 405-413.

REPORT DOCUMENTATION PAGE

Form Approved
OMB No. 0704-0188

1. AGENCY USE ONLY (*Leave blank*)	2. REPORT DATE	3. REPORT TYPE AND DATES COVERED
	July 1997	Technical Memorandum

4. TITLE AND SUBTITLE

Study of CFD Methods Applied to Rapidly Deforming Boundaries

5. FUNDING NUMBERS

WU–509–10–51

6. AUTHOR(S)

John W. Slater, Donald Freund, and Miklos Sajben

7. PERFORMING ORGANIZATION NAME(S) AND ADDRESS(ES)

National Aeronautics and Space Administration
Lewis Research Center
Cleveland, Ohio 44135–3191

8. PERFORMING ORGANIZATION REPORT NUMBER

E–10775

9. SPONSORING/MONITORING AGENCY NAME(S) AND ADDRESS(ES)

National Aeronautics and Space Administration
Washington, DC 20546–0001

10. SPONSORING/MONITORING AGENCY REPORT NUMBER

NASA TM–107482
AIAA–97–2041

11. SUPPLEMENTARY NOTES

Prepared for the 13th Computational Fluid Dynamics Conference sponsored by the American Institute of Aeronautics and Astronautics, Snowmass Village, Colorado, June 29—July 2, 1997. John W. Slater, NASA Lewis Research Center; Donald Freund and Miklos Sajben, University of Cincinnati, Department of Aerospace Engineering and Engineering Mechanics, Cincinnati, Ohio. Responsible person, John W. Slater, organization code 5850, (216) 433–8513.

12a. DISTRIBUTION/AVAILABILITY STATEMENT

Unclassified - Unlimited
Subject Categories ~~01~~ and ~~07~~ 34

This publication is available from the NASA Center for AeroSpace Information, (301) 621–0390.

12b. DISTRIBUTION CODE

13. ABSTRACT (*Maximum 200 words*)

A study of various methods of computational fluid dynamics (CFD) was performed to understand their effects on the analysis of the flow field induced by the rapid collapse of a flexible bump in an annular duct with initially stagnant conditions. This flow represents a good test case for CFD methods for deforming boundaries because the flow is due entirely to the boundary motion. The study examined methods for implementing explicit and implicit time integration, modeling the bump collapse, imposing moving surface boundary conditions, modeling the grid dynamics, computing the numerical flux, and imposing the geometric conservation law. Good agreement was obtained between the CFD results and the time-varying static pressure readings obtained from an experiment. Significant results showed the crucial importance of the bump collapse model and the wall boundary conditions. The geometric conservation law was not of critical importance.

14. SUBJECT TERMS

Computational fluid dynamics; Unsteady flow; Moving geometry; Variable geometry

15. NUMBER OF PAGES

12

16. PRICE CODE

A03

17. SECURITY CLASSIFICATION OF REPORT	18. SECURITY CLASSIFICATION OF THIS PAGE	19. SECURITY CLASSIFICATION OF ABSTRACT	20. LIMITATION OF ABSTRACT
Unclassified	Unclassified	Unclassified	